

Significance of matrix diagonalization in modelling inelastic electron scattering



Z. Lee^{a,*}, R. Hambach^{a,b}, U. Kaiser^a, H. Rose^a

^a University of Ulm, Ulm 89081, Germany

^b University of Jena, Jena 07743, Germany

ARTICLE INFO

Keywords:

Inelastic scattering

MDFF

Matrix diagonalization

ABSTRACT

Electron scattering is always applied as one of the routines to investigate nanostructures. Nowadays the development of hardware offers more and more prospect for this technique. For example imaging nanostructures with inelastic scattered electrons may allow to produce component-sensitive images with atomic resolution. Modelling inelastic electron scattering is therefore essential for interpreting these images. The main obstacle to study inelastic scattering problem is its complexity. During inelastic scattering, incident electrons entangle with objects, and the description of this process involves a multidimensional array. Since the simulation usually involves fourdimensional Fourier transforms, the computation is highly inefficient. In this work we have offered one solution to handle the multidimensional problem. By transforming a high dimensional array into twodimensional array, we are able to perform matrix diagonalization and approximate the original multidimensional array with its twodimensional eigenvectors. Our procedure reduces the complicated multidimensional problem to a twodimensional problem. In addition, it minimizes the number of twodimensional problems. This method is very useful for studying multiple inelastic scattering.

1. Introduction

Electron scattering has been applied as a conventional method for determining and imaging nanostructures since several decades. Modelling electron scattering is essential for interpreting electron microscopy images. The main obstacle for a quantitative analysis is the strong interaction between electron beam and target. Only in case of high-energy electron wave ≥ 100 keV propagating through atomically thin specimens, the scattered electron wave can be described as a simple product of the incident electron wave and an object transmission function. This so-called phase-object approximation (POA) completely neglects dynamical effects, inelastic scattering, and backscattering [1].

For thick samples, dynamical effects become important, i.e., electrons are scattered several times resulting in complicated interference patterns in the image. Multiple elastic scattering within a thick sample is usually simulated by employing either the Bloch-wave formalism [2] or the multislice algorithm [3]. In the latter method, the sample is sliced into thin layers and the static sample potential in each slice is projected along the optical axis onto a plane. The propagation of the incident electron wave through each of these planes is modelled by the POA, while the propagation between adjacent slices is described by the Fresnel propagator of vacuum. As the latter is most

conveniently evaluated in reciprocal space, the multislice method generally requires two *two*-dimensional Fourier transforms at each slice.

For slow electrons accelerated by low voltages like 20 kV, the interaction between beam and target electrons becomes so strong that inelastic scattering must be taken into account [4]. In this case, energy is transferred from the scattering electron to the target, which gets excited from its initial ground state. This entangles the electron with the target, i.e., in contrast to elastic scattering, one can no longer describe the outgoing electron by a single wave function. Instead, one has to consider many partial waves, which are only coherent if they belong to the same excited object state and are otherwise incoherent. Equivalently, one can employ the concept of the density matrix, or mutual coherence function (MCF), to describe the partial coherence of inelastic scattered electrons [5–8]. For thin samples and a single inelastic scattering event, the outgoing MCF is the product of the incident MCF and the mutual dynamic object transparency (MDOT) of the target. The MDOT can be understood as an extension of the standard object transmission function used in the POA [5]. It includes both elastic and inelastic scattering and depends on four spatial coordinates plus time. For thick samples, multiple scattering has to be included and the multislice algorithm has been extended to include also inelastic scattering [9–11]. The MCF is then propagated through

* Corresponding author.

the sliced object, where the scattering in each layer is represented by the corresponding MDOT of the slice. Unfortunately, this method is computationally *very* expensive: First, the propagation of the MCF involves *four*-dimensional Fourier transforms at each slice and for each excitation energy. And second, the MDOT can be only computed for simple model systems or using severe approximations for the inelastic part of the MDOT. The latter is basically given by the (inelastic) mixed dynamic form factor (MDFF) of the target, which reads in reciprocal space as [5,6]

$$S(\vec{q}, \vec{q}', E) = \sum_{j=1}^{\infty} \langle 0 | \hat{n}(\vec{q}) | j \rangle \langle j | \hat{n}(-\vec{q}') | 0 \rangle \delta(E - E_j + E_0). \quad (1)$$

Here \vec{q} and \vec{q}' are two-dimensional reciprocal vectors perpendicular to the beam (each conjugate to two spatial coordinates in the MDOT) and E is the energy transferred to the target (conjugate to the time variable in the MDOT). The summation runs over all excited states $|j\rangle$ of the target with corresponding energy E_j , while $|0\rangle$ denotes the initial ground state with energy E_0 . Thus, the MDFF contains information about all possible excitations in the many-electron system. More precisely, the delta-function enforces conservation of energy and the matrix elements of the density operator \hat{n} measure the electron-density fluctuations due to the excitation. The calculation of the MDFF thus requires the solution of a complicated quantum-mechanical many-body problem. As the MDFF is intimately related to the density-density correlation function [6], (time-dependent) density functional theory [12] can be used to calculate the MDFF from first-principles. Even for simple systems like a perfect silicon crystal, this approach requires a huge computational effort and has been rarely used for simulations [13].

Several approximations for the MDFF and the propagation of the beam are employed in literature to reduce the complexity of the computation (see, e.g., [14,15] and references therein):

(i) First, the MDFF is generally calculated using an effective single-particle picture, i.e., many-body effects in the excitation of the target are completely neglected. For large excitation energies, single atoms of the target are often considered to be independent, such that Eq. (1) reduces to a simple sum over ‘atomic orbitals’. Also phenomenological models, combining the measured electron energy-loss spectrum with the dipole approximation of the MDFF [16] or the Raman-Compton model [4], have been used successfully when a detailed knowledge of the distribution of inelastic scattering angles is not necessary.

(ii) Second, only a single inelastic scattering event is included in the simulation, while multiple elastic scattering is fully taken into account. The propagation of the external electron can thus be separated into three parts: an elastic propagation to a certain slice at depth z_i , an inelastic scattering (at an atom) within this slice, and a subsequent elastic propagation through the rest of the specimen. Assuming that the inelastic scattering event occurs with the same probability in any sample slice, the calculation is repeated for all possible positions and the results are averaged incoherently. Note that the emission volume of the inelastic scattered electron is implicitly limited along the beam direction by the thickness of one slice. If one is interested in low-energy excitations, like plasmons, this restriction can be circumvented using a backpropagation method [7].

(iii) Third, instead of employing a two-point quantity, like the density matrix $\rho(\vec{r}, \vec{r}')$ or MCF, to describe the partial coherence of the electron beam, a finite number N of partial waves $\phi_n(\vec{r})$ is propagated through the system. For each partial wave, a fully coherent (standard) multislice calculation is performed through the system. In the case of high-resolution imaging on the transmission electron microscope, the propagated partial waves are convoluted with the optic transfer function of the microscope and the resulting N images are averaged incoherently at the detector. As a result, the 4D Fourier transforms in the propagation of the MCF are replaced by 2D Fourier transforms for N partial waves. The efficiency of this approach depends

on the number of required partial waves, i.e., the incoherence of the beam [14,16–19].

In principle, an infinite number of mutually incoherent partial waves is needed for the representation of an arbitrary density matrix: $\rho(\vec{r}, \vec{r}') = \sum_n \phi_n(\vec{r}) \phi_n^*(\vec{r}')$. The aim of this article is to assess how many partial waves are generally needed for modelling inelastic electron scattering, and try to replace the 4D Fourier transforms required for computing the scattered waves by a minimum number of 2D Fourier transforms. We will employ a very simple and phenomenological model for the MDFF and consider the EFTM imaging for a single atom and a crystal at low and high energy loss.

2. How matrix diagonalization is employed to simplify the inelastic scattering problem

Simultaneous elastic and inelastic scattering in a thin sample is modelled by the product of incident wave and the MDOT $\gamma(\vec{\rho}, \vec{\rho}', \Delta E)$ [5]. Our current model assumes multiple elastic scattering and one inelastic scattering. Under this condition, the MDOT is approximated by [5]

$$\begin{aligned} \gamma(\vec{\rho}, \vec{\rho}', \Delta E) &= \exp \left[i\Phi(\vec{\rho}) - i\Phi(\vec{\rho}') - \frac{1}{2}\mu_2(\vec{\rho}) - \frac{1}{2}\mu_2(\vec{\rho}') \right. \\ &\quad \left. + \mu_{11}(\vec{\rho}, \vec{\rho}', \Delta E) \right] \\ &\approx \exp \left[i\Phi(\vec{\rho}) - i\Phi(\vec{\rho}') - \frac{1}{2}\mu_2(\vec{\rho}) - \frac{1}{2}\mu_2(\vec{\rho}') \right] \\ &\quad \times [a_0 + b_0\mu_{11}(\vec{\rho}, \vec{\rho}', \Delta E)]. \end{aligned} \quad (2)$$

Here $\exp[i\Phi(\vec{\rho})]$ represents the POA. $\mu_2(\vec{\rho})$ and $\mu_2(\vec{\rho}')$ correspond to absorption of elastically scattered electrons, and $\mu_{11}(\vec{\rho}, \vec{\rho}', \Delta E)$ represents the transmission of inelastic scattered electrons. a_0 and b_0 are two constants determined by fitting of the function $\exp[\mu_{11}] \approx a_0 + b_0\mu_{11}$ in the vicinity of μ_{11} . In the case that $\mu_{11} \ll 1$, one obtains $a_0 = b_0 = 1$.

In the case of normal incidence on the sample surface, the quantity $\mu_{11}(\vec{\rho}, \vec{\rho}', \Delta E)$ and $\mu_2(\vec{\rho})$ are associated with the MDFF by [5]

$$\mu_{11}(\vec{\rho}, \vec{\rho}', \Delta E) = \left(\frac{\alpha_s}{\pi\beta} \right)^2 \iint \frac{S(\vec{q}, \vec{q}', \Delta E)}{(q_E^2 + q^2)(q_E^2 + q'^2)} e^{i\vec{q}\vec{\rho}} e^{-i\vec{q}'\vec{\rho}'} d^2\vec{q} d^2\vec{q}' \quad (3)$$

$$\mu_2(\vec{\rho}) = \int \mu_{11}(\vec{\rho} = \vec{\rho}', \Delta E) p(\Delta E) d\Delta E \quad (4)$$

Here $\alpha_s = 1/137$ is the Sommerfeld constant. $\beta = v/c$ is the ratio between the velocity of the incident electron v and velocity of light c . $p(\Delta E)$ is the normalized energy-loss spectra. The characteristic inelastic scattering vector $q_E = 2\pi\theta_E/\lambda$ is determined by the incident wavelength λ and the characteristic inelastic scattering angle θ_E :

$$\theta_E = \frac{\Delta E}{\beta^2(E_0 + m_e c^2)}. \quad (5)$$

Here ΔE is the energy loss of the incident electron, and m_e is the non-relativistic electron mass.

According to the relation in Eq. (3), a 4D Fourier transform is required for determining μ_{11} . By means of matrix diagonalization introduced in Appendix A, we can decompose the function $\frac{S(\vec{q}, \vec{q}', \Delta E)}{(q_E^2 + q^2)(q_E^2 + q'^2)}$ as combination of eigenvectors depending on \vec{q} and \vec{q}' , respectively. We obtain

$$\frac{S(\vec{q}, \vec{q}', \Delta E)}{(q_E^2 + q^2)(q_E^2 + q'^2)} = \sum_n \lambda_n \phi_n(\vec{q}, \Delta E) \phi_n^*(\vec{q}', \Delta E). \quad (6)$$

Here $\phi_n(\vec{q}, \Delta E)$ and $\phi_n(\vec{q}', \Delta E)$ are the orthonormal eigenvectors; λ_n is a real eigenvalue.

Substituting Eq. (6) into Eq. (3), we obtain the diagonal form of the

function μ_{11} denoting inelastic scattering:

$$\begin{aligned}\mu_{11}(\vec{\rho} \rightarrow \vec{\rho}', \Delta E) &= \left(\frac{\alpha_s}{\pi\beta}\right)^2 \sum_n \lambda_n \left| \int \phi_n(\vec{q}, \Delta E) e^{i\vec{q}\vec{\rho}} d^2\vec{q}_\rho \right|^2 \\ &= \left(\frac{\alpha_s}{\pi\beta}\right)^2 \sum_n \lambda_n |\phi_n(\vec{\rho}, \Delta E)|^2.\end{aligned}\quad (7)$$

Eq. (7) indicates, the 4D Fourier transform required to model inelastic electron scattering reduces to the combination of 2D Fourier transforms. The number of 2D Fourier transforms depends on the number of necessary eigenvectors required to decompose the original 4D quantity. We introduce the transmission function t_n for each eigenvector according to Eqs. (2) and (7):

$$t_n(\vec{\rho}, \Delta E) = \frac{\alpha_s \sqrt{b_0}}{\pi\beta} \exp[i\Phi(\vec{\rho}) - \mu_2(\vec{\rho})] \sqrt{\lambda_n} \phi_n(\vec{\rho}, \Delta E). \quad (8)$$

Ignoring the optical transfer system, we obtain the image of a thin sample formed by inelastic scattered electrons with an energy loss of ΔE simply as

$$I(\vec{\rho}, \Delta E) = \sum_n |\psi_0(\vec{\rho}) t_n(\vec{\rho}, \Delta E)|^2 \quad (9)$$

Here $\psi_0(\vec{\rho})$ denotes the incident wave. Eq. (9) shows that the final image should be an incoherent summation of the scattered partial waves calculated by the products of the incident wave ψ_0 and the transmission function t_n .

However, not all terms are equally large. The magnitude of the eigenvalue λ_n determines the average contribution of each term. Generally, a large eigenvalue λ_n indicates an important contribution of the eigenvector $\phi_n(\vec{q}, \Delta E)$. By considering only the dominating terms, we can approximate the MDFF with a few eigenvectors. As a result, the 4D Fourier transform in Eq. (3) is replaced by a summed products of a small number of 2D Fourier transforms. For the simulation of an EFTEM image using multislice algorithm, one needs to compute a pair of 4D Fourier transform at each slice and a series of 4D Fourier transforms for each energy loss, which can be very time-consuming. Converting 4D Fourier transforms to only a few of 2D Fourier transforms in this case is computationally preferred.

3. Examples

In order to find out the optimum eigenvectors for representing the MDFF, we use the MDFF derived from the modified Raman-Compton approximation and the Wentzel model [4] for illustration.

The Raman-Compton model is written as

$$S(\vec{K}, \vec{K}', \Delta E) \approx p(\Delta E) [F(\vec{K} - \vec{K}') - \frac{1}{Z} F(\vec{K}) F(-\vec{K}')]. \quad (10)$$

Here \vec{K} and \vec{K}' are the scattering vectors; Z is the atomic number; ΔE represents the energy loss results from the inelastic scattering; $p(\Delta E)$ is the energy-loss spectra of a single atom; F is the atomic form factor.

The Raman-Compton model (Eq. (10)) accounts for the entanglement of the incident electron and the object atom as a result of inelastic scattering. However, this model neglects the interactions between the electrons of the single atom. When this model is applied for a crystal, the interatomic interactions are neglected as well, and the MDFF for a crystal is simply calculated as a superposition of the MDFFs of single atoms. Despite all these assumptions, this model offers a surprisingly good approximation. For small scattering angles, the Raman-Compton model coincides with the dipole approximation. For high scattering angles, the Raman-Compton model includes a cutoff so that inelastic scattering is negligible for scattering angle larger than the characteristic inelastic scattering angle θ_E . This behavior is consistent with that obtained from the homogeneous electron gas model [20].

Another advantage of the Raman-Compton model is that the rather involved electron-object entanglement can be calculated from the

atomic form factors of single atoms. Here we have applied Wentzel model [21] for this purpose. The Wentzel potential employs single-atom approximation and includes a screening factor which shields the electron from the positive potential of the nucleus if the distance between them is more than twice the screening radius. The Wentzel model is a good approximation for describing the potential distribution in a conductor.

Combining the Raman-Compton model for the MDFF and the Wentzel model for calculating the atomic form factor, we obtain the approximated MDFF for a single atom used in our examples:

$$S(\vec{q}, \vec{q}', \Delta E) = Z \left[\frac{q_A^2}{q_A^2 + (\vec{q} - \vec{q}')^2} - \frac{q_A^2}{q_A^2 + q_E^2 + q^2} \frac{q_A^2}{q_A^2 + q_E^2 + q'^2} \right] p(\Delta E) \quad (11)$$

Here the characteristic elastic scattering vector q_A is the reciprocal of the screening radius, and q_E is the characteristic inelastic scattering vector.

For a crystal, the MDFF is obtained by summing up the MDFFs of single atoms:

$$\begin{aligned}S(\vec{q}, \vec{q}', \Delta E) &= p(\Delta E) \sum_\nu e^{-i(\vec{q} - \vec{q}') \cdot \vec{\rho}_\nu} \left[\frac{q_{A\nu}^2}{q_{A\nu}^2 + (q_\nu - q_\nu')^2} \right. \\ &\quad \left. - \frac{q_{A\nu}^2}{q_{A\nu}^2 + q_E^2 + q_\nu^2} \frac{q_{A\nu}^2}{q_{A\nu}^2 + q_E^2 + q_\nu'^2} \right].\end{aligned}\quad (12)$$

Here $\vec{\rho}_\nu$ is the positional vector of the ν th atom.

The numerical diagonalization of a 4D Hermitian matrix or symmetric matrix follows three steps: i) Flatten the 4D matrix so that it becomes 2D; ii) Retrieve the eigenvalues and eigenvectors by means of matrix diagonalization; iii) Restore the eigenvectors from 1D back to 2D. A detailed description is found in Appendix A. In the following the diagonalization of the MDFF is performed for low and high energy loss, in the cases of a single atom and a crystal. Carbon materials are used as typical examples.

3.1. Single atom

The mixed dynamic form factor obtained by the Raman-Compton-Wentzel model for a single atom (Eq. (11)) can be written in Cartesian coordinates as

$$\begin{aligned}S(\vec{q}, \vec{q}', \Delta E) &= S(q_x, q_y, q'_x, q'_y, \Delta E) \\ &= Z \left[\frac{q_A^2}{q_A^2 + (q_x - q'_x)^2 + (q_y - q'_y)^2} \right. \\ &\quad \left. - \frac{q_A^2}{q_A^2 + q_E^2 + q_x^2 + q_y^2} \frac{q_A^2}{q_A^2 + q_E^2 + q_x'^2 + q_y'^2} \right] p(\Delta E).\end{aligned}\quad (13)$$

A grid of the size $50 \text{ \AA} \times 50 \text{ \AA}$ is chosen to map the potential of a carbon atom, sampled by 80×80 pixels. The origin is set at the center of the grid. The length 50 \AA guarantees that the atomic potential drops close to zero at the edge of the grid. This behavior avoids alias effect, i.e. contributions from periodically repeated 'neighbour' atoms when one performs the Fourier transform. Accordingly, the four-dimensional array is defined by the size $50 \text{ \AA} \times 50 \text{ \AA} \times 50 \text{ \AA} \times 50 \text{ \AA}$, mapped by $80 \times 80 \times 80 \times 80$ pixels. This arrangement determines a sampling of 0.625 \AA/px in real space and $0.02 \text{ \AA}^{-1}/\text{px}$ in reciprocal space. One should bear in mind that for an $N \times N \times N \times N$ array, the flattened matrix is of the size $N^2 \times N^2$ and it can be time-consuming for retrieving the eigenvalues and eigenvectors if N^2 is too large.

3.1.1. Low-loss

We assume that a 20 keV incident electron is scattered by a single carbon atom and suffers an energy loss of $\Delta E = 10 \text{ eV}$. The nine largest

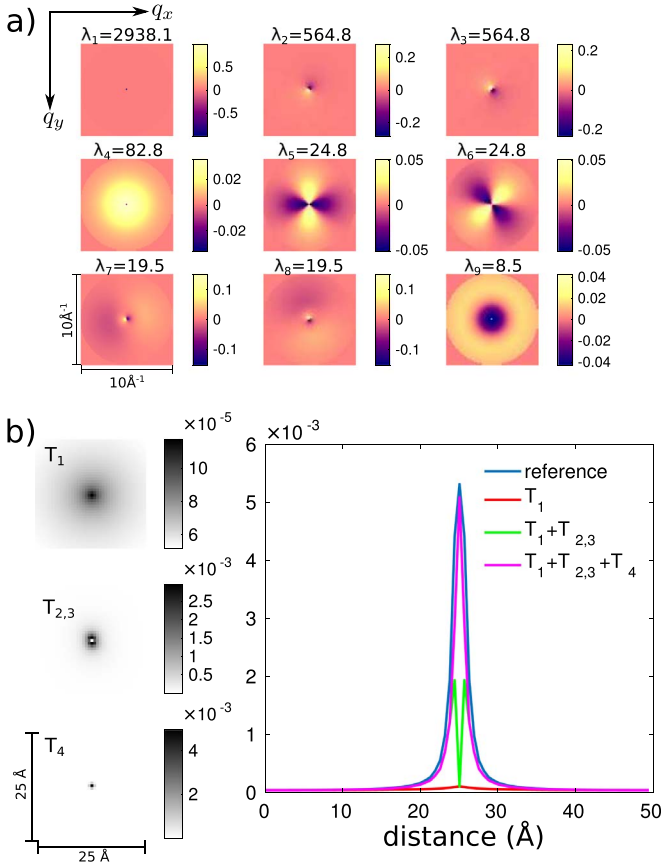


Fig. 1. a) The first nine reshaped eigenvectors $\phi_n(\vec{q})$ of the matrix $S(\vec{q}, \vec{q}', \Delta E)/[(q_E^2 + q^2)(q_E'^2 + q'^2)]$ accounting for a 20 keV electron wave scattered by a single carbon atom and resulting in an energy loss of 10 eV. Here the characteristic elastic scattering vector $q_A = 3.43 \text{ \AA}^{-1}$ and the characteristic inelastic scattering vector $q_E = 0.018 \text{ \AA}^{-1}$. The corresponding eigenvalues are listed above the map of each eigenvector. b) Left: Contributions of the first four eigenvectors to the term μ_{11} calculated based on Eq. (14). Right: Diagonal elements $\mu_{11}(\vec{\rho} = \vec{\rho}', \Delta E = 10 \text{ eV}, E_0 = 20 \text{ keV})$ for a single carbon atom calculated I) by the 4D Fourier transform following Eq. (3) (blue line) and II) by the sum of 2D Fourier transforms (Eq. (7)) of the eigenvectors obtained from matrix diagonalization. The partial sums show that the first four terms provide a good approximation.

eigenvalues of the term $S(\vec{q}, \vec{q}', \Delta E)/[(q_E^2 + q^2)(q_E'^2 + q'^2)]$ in Eq. (6) are retrieved based on the Lanczos algorithm [22] and marked in Fig. 1 a) above their corresponding eigenvectors, respectively. Since the contribution of each eigenvector is closely related with the magnitude of the corresponding eigenvalue, we can neglect eigenvectors if the accordant eigenvalues are negligibly small compared with the largest eigenvalue. According to the values $\lambda_1 - \lambda_9$ listed above, it is necessary to keep the first four eigenvectors for approximating the original function.

In order to verify the dominant terms of Eq. (7), we calculated the contribution of these eigenvectors to the function $\mu_{11}(\vec{\rho} = \vec{\rho}')$ based on Eq. (7) (Fig. 1b). We summed up the terms corresponding to the same eigenvalue and define the individual contributions as T_1 , $T_{2,3}$ and T_4 :

$$T_1 = \left(\frac{\alpha_s}{\pi\beta}\right)^2 \lambda_1 |\phi_1(\vec{\rho})|^2, T_{2,3} = \left(\frac{\alpha_s}{\pi\beta}\right)^2 \sum_{n=2}^3 \lambda_n |\phi_n(\vec{\rho})|^2, T_4 = \left(\frac{\alpha_s}{\pi\beta}\right)^2 \lambda_4 |\phi_4(\vec{\rho})|^2. \quad (14)$$

The plot in Fig. 1b) shows the diagonal elements of μ_{11} for a single carbon atom imaged at 20 kV with an energy loss of $\Delta E = 10 \text{ eV}$, calculated with two methods - 1. The 4D Fourier transform (Eq. (3)) denoted by the blue line; 2. The sum of 2D Fourier transforms (Eq. (7)) of the eigenvectors obtained from matrix diagonalization. Fig. 1b) demonstrates that the sum of the first four terms provide a sufficient

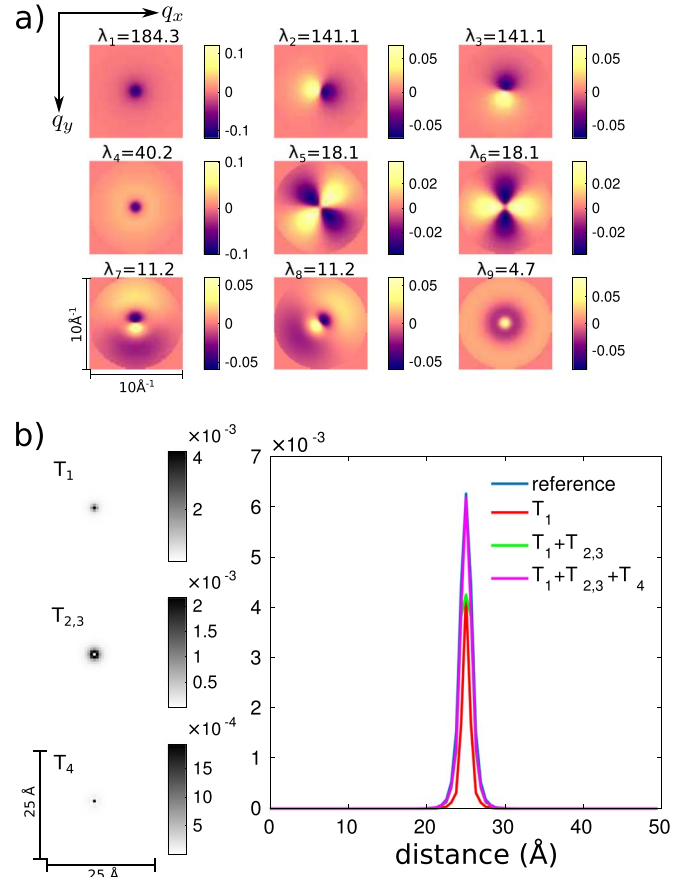


Fig. 2. a) The first nine reshaped eigenvectors $\phi_n(\vec{q})$ of the matrix $S(\vec{q}, \vec{q}', \Delta E)/[(q_E^2 + q^2)(q_E'^2 + q'^2)]$ accounting for a 20 keV electron scattered by a single carbon atom and resulting in an energy loss of 300 eV. Here the characteristic elastic scattering vector is $q_A = 3.43 \text{ \AA}^{-1}$ and the characteristic inelastic scattering vector is $q_E = 0.56 \text{ \AA}^{-1}$. The corresponding eigenvalues are listed above the map of each eigenvector. b) Left: Contributions of the first four eigenvectors to the term μ_{11} calculated based on Eq. (14). Right: Diagonal elements $\mu_{11}(\vec{\rho} = \vec{\rho}', \Delta E = 300 \text{ eV}, E_0 = 20 \text{ keV})$ for a single carbon atom calculated I) by the 4D Fourier transform following Eq. (3) (blue line) and II) by the sum of 2D Fourier transforms of the eigenvectors obtained from matrix diagonalization (Eq. (7)). The partial sums show that the first four terms provide a good approximation.

approximation of the exact μ_{11} calculated by using the 4D Fourier transform. It is also worth mentioning that the peak value in the partial image T_1 corresponding to the largest eigenvalue λ_1 is two orders smaller than those in $T_{2,3}$ and T_4 . Instead, T_1 is much more dispersively distributed than T_2 and T_3 . This demonstrates that a high eigenvalue solely does not secure high local values in μ_{11} . Especially in the case when fine resolution needs to be achieved, one should not judge the necessity of the eigenvectors only by the magnitude of the corresponding eigenvalues.

In addition, the eigenvectors of the term $S(\vec{q}, \vec{q}', \Delta E)/[(q_E^2 + q^2)(q_E'^2 + q'^2)]$ for a single atom resemble a series of spherical harmonics expansion (Fig. 1), and we will discuss the phenomenon in Section 4.2.

3.1.2. Core-loss

As an example for core-loss excitation, we consider a single carbon atom scattering a 20 keV electron, which results in an energy loss of 300 eV for the incident electron. The corresponding matrix $S(\vec{q}, \vec{q}', \Delta E)/[(q_E^2 + q^2)(q_E'^2 + q'^2)]$ is diagonalized and the largest 9 eigenvalues as well as the eigenvectors are shown in Fig. 2 a). The contributions of the first four eigenvectors to the function μ_{11} are evaluated and compared with the μ_{11} calculated with 4D Fourier transform (Eq. (3)), as shown in Fig. 2b). Similar to the case of low energy loss ($\Delta E = 10 \text{ eV}$), the first four eigenvectors approximate

$S(\vec{q}, \vec{q}', \Delta E = 300 \text{ eV}) / [(q_E^2 + q^2)(q_E^2 + q'^2)]$ with a sufficient degree of accuracy. As a short summary, the 4D matrix $S(\vec{q}, \vec{q}', \Delta E) / [(q_E^2 + q^2)(q_E^2 + q'^2)]$ is employed to calculate the inelastic transmission function and the calculation involves a 4D Fourier transform. In the case of a single carbon atom scattering a 20 keV electron, the 4D matrix can be approximated with four of its 2D eigenvectors, valid for both low and high energy loss. This indicates, an inelastic scattering by a single carbon atom can now be modelled with four 2D functions, instead of one 4D function. Correspondingly, each 4D Fourier transform required for calculating the propagation of the scattered waves can be approximated by four 2D Fourier transforms.

3.2. Crystal

As an example for crystals, graphene is chosen to illustrate the diagonalization of the term $S(\vec{q}, \vec{q}', \Delta E) / [(q_E^2 + q^2)(q_E^2 + q'^2)]$. In our model, the MDFF for a crystal is calculated by summing up the MDFF of each individual atom based on Eq. (12). Two graphene cells are sampled with 70x80 pixels. This configuration results in a sampling of 0.12 Å/px in real space and 0.1 Å⁻¹/px in reciprocal space, which provides sufficient resolvability in both real and reciprocal space. The diagonalization of the 4D matrix $S(\vec{q}, \vec{q}', \Delta E) / [(q_E^2 + q^2)(q_E^2 + q'^2)]$ follows the approach introduced in Appendix A, and the results for low-loss and core-loss are discussed as follows.

3.2.1. Low-loss

In the low-loss example, we assume that a beam of 20 keV electrons are scattered by a thin layer of graphene, and suffer an energy loss of 10 eV. In this case, the first three eigenvectors resulting from the matrix diagonalization of $S(\vec{q}, \vec{q}', \Delta E) / [(q_E^2 + q^2)(q_E^2 + q'^2)]$ are shown in Fig. 3a). Unlike the example of a single atom, the eigenvectors in this case consist of reflections showing certain symmetries. The first eigenvalue $\lambda_1 = 3 \times 10^6$ is almost 10⁵ times larger than the second

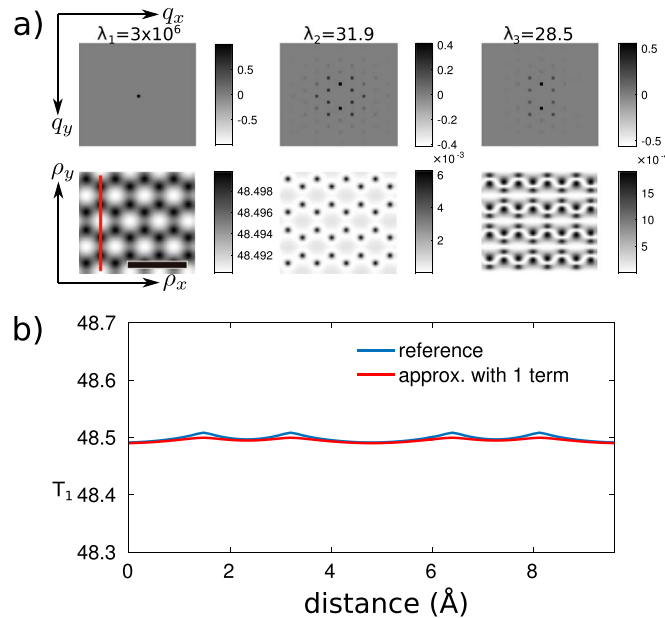


Fig. 3. a) 1st row: Real parts of the first three eigenvectors of the 4D matrix $S(\vec{q}, \vec{q}', \Delta E) / [(q_E^2 + q^2)(q_E^2 + q'^2)]$ assuming a beam of 20 keV electrons scattered by graphene and resulting in an energy loss of 10 eV. The corresponding eigenvalues are listed above each eigenvector. 2nd row: the contributions of the first three eigenvectors to the quantity μ_{11} calculated based on Eq. (7). b) The diagonal elements $\mu_{11}(\vec{\rho} = \vec{\rho}', \Delta E = 10 \text{ eV}, E_0 = 20 \text{ keV})$ for graphene calculated with two methods - 4D Fourier transform following Eq. (3) (blue curve) and 2D Fourier transform (Eq. (7)) of one eigenvector corresponding to the largest eigenvalue obtained from matrix diagonalization (red curve). The $\mu_{11}(\vec{\rho} = \vec{\rho}', \Delta E = 10 \text{ eV})$ is close to a constant for graphene. Scale bar: 0.5 nm.

largest eigenvalue $\lambda_2 = 31.9$, and its corresponding eigenvector resembles a delta function (Fig. 3 1st image in the 1st row). An optimistic conjecture would be that one single eigenvector is sufficient for approximating the 4D matrix. In order to verify our surmise, we have calculated the contributions of the first three eigenvectors to the quantity $\mu_{11}(\vec{\rho} = \vec{\rho}')$ based on Eq. (7), as shown in the second row of Fig. 3a). Judging from the scale bars of the three plots, we come to the conclusion that the first eigenvector is dominantly strong. Especially, since the first eigenvector $\phi_1(\vec{q}, \Delta E)$ resembles a delta peak, its contribution to the term μ_{11} calculated from the Fourier transform (Eq. (7)) is close to a constant. Fig. 3b) shows the diagonal elements of μ_{11} for graphene calculated with 4D Fourier transform in blue (Eq. (3)) and the approximation using the first eigenvector obtained by matrix diagonalization (red curve). Both curves are close to a constant value. This indicates, low-loss scattering in a crystal is highly delocalized and one eigenvector suffices for reconstructing the original 4D function $S(\vec{q}, \vec{q}', \Delta E) / [(q_E^2 + q^2)(q_E^2 + q'^2)]$.

As a result, low-loss scattering within a thin sample can be modelled by the product of incoming wave and a 2D function. The multislice method incorporating elastic and inelastic scattering in a thick object is recapitulated in Fig. 4.

Electron wave propagating through the slices is formulated by Eq. (15):

$$\psi_n(\vec{\rho}) = [\psi_{n-1}(\vec{\rho}) \cdot t_n(\vec{\rho})] \otimes P(\vec{\rho}) \quad (15)$$

Here $t_n(\vec{\rho})$ is the transmission function of the n th slice of the object and $P(\vec{\rho})$ is the Fresnel propagator. Inelastic scattering takes place at the m th slice. Above and below this slice, the transmission function $t_n(\vec{\rho})$ employs the POA:

$$t_n(\vec{\rho}) = \exp[i\Phi_n(\vec{\rho})]. \quad (16)$$

Within the m th layer, the wave splits into two parts - one part is elastically scattered, and the other part is inelastic scattered. According to Eqs. (2)–(3), the transmission functions $t^{(el)}(\vec{\rho})$ for elastic scattering and $t^{(in)}(\vec{\rho}, \Delta E)$ for inelastic scattering are written separately as

$$t_m^{(el)}(\vec{\rho}) = \frac{\alpha a_0}{\pi \beta} \exp[i\Phi_m(\vec{\rho}) - \mu_2(\vec{\rho})], \quad (17)$$

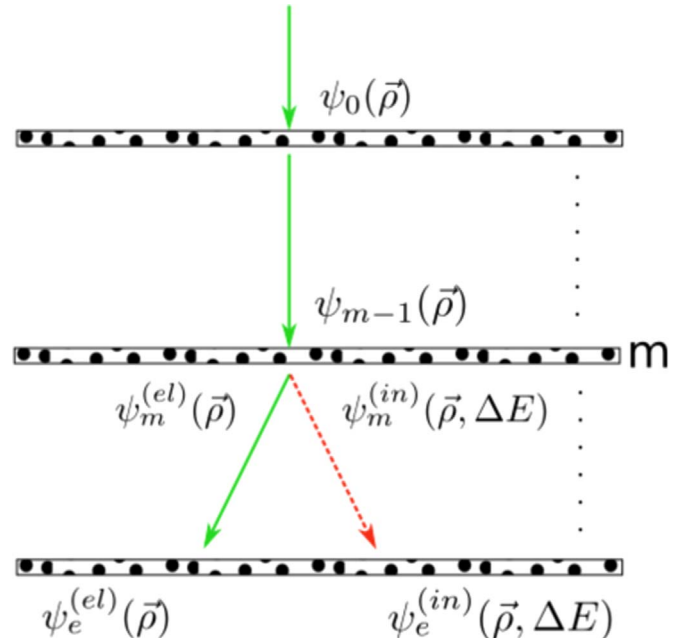


Fig. 4. A sketched procedure for multislice calculation involving inelastic scattering at the m th layer. The scattered wave splits into two parts - elastically scattered wave $\psi_m^{(el)}(\vec{\rho})$ and inelastic scattered wave $\psi_m^{(in)}(\vec{\rho}, \Delta E)$.

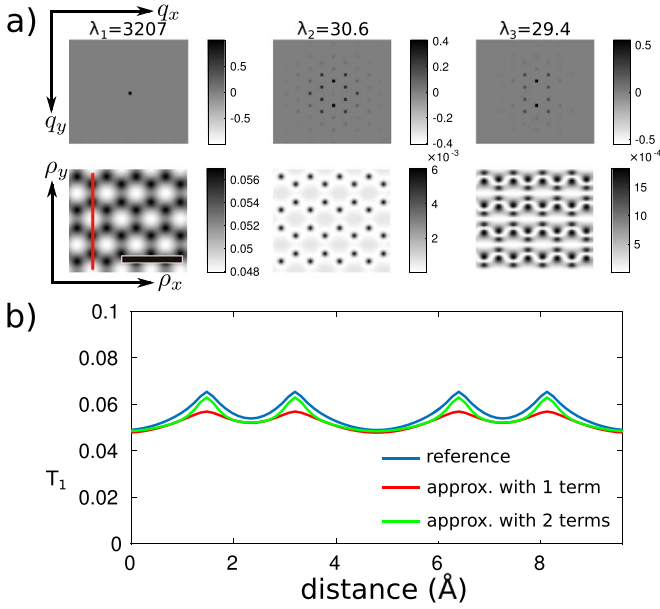


Fig. 5. a) 1st row: Real parts of the first three reshaped eigenvectors of the matrix $S(\vec{q}, \vec{q}', \Delta E)/[(q_E^2 + q^2)(q_E^2 + q'^2)]$ assuming a beam of 20 keV electrons scattered by graphene and resulting in an energy loss of 300 eV. The corresponding eigenvalues are listed above each eigenvector. 2nd row: the contributions of the first three eigenvectors to the quantity μ_{11} calculated based on Eq. (7). b) The diagonal elements $\mu_{11}(\vec{\rho} = \vec{\rho}', \Delta E = 300 \text{ eV}, E_0 = 20 \text{ keV})$ for graphene calculated with two methods - 4D Fourier transform following Eq. (3) (blue curve) and 2D Fourier transform (Eq. (7)) of one eigenvector (red curve), or of two eigenvectors (green curve). Scale bar: 0.5 nm.

$$t_m^{(in)}(\vec{\rho}, \Delta E) = \frac{\alpha\sqrt{b_0}}{\pi\beta} \exp[i\Phi_m(\vec{\rho}) - \mu_2(\vec{\rho})] \sqrt{\lambda_1} \phi_1(\vec{\rho}, \Delta E). \quad (18)$$

As a short summary, low-loss scattering is incorporated in the conventional multislice algorithm by assuming that the low-loss scattering takes place at a certain layer of the sample. The transmission function $t_m^{(in)}(\vec{\rho}, \Delta E)$ for inelastic scattering is introduced, which is a product of the transmission function $t_m^{(el)}(\vec{\rho})\phi_1(\vec{\rho}, \Delta E)$ for elastic scattering and a 2D function $\sqrt{\lambda_1}\phi_1(\vec{\rho}, \Delta E)$. The 2D function $\sqrt{\lambda_1}\phi_1(\vec{\rho}, \Delta E)$ is close to a constant, since it is calculated from the Fourier transform of the corresponding eigenvector $\phi_1(\vec{q}, \Delta E)$ (Eq. (7)), which resembles a delta function as shown in the upper left image in Fig. 3 a).

3.2.2. Core-loss

In the case when the scattering of 20 keV electrons by a thin graphene layer results in an energy loss of 300 eV, the largest eigenvalue obtained from the diagonalization of the corresponding 4D matrix $S(\vec{q}, \vec{q}', \Delta E)/[(q_E^2 + q^2)(q_E^2 + q'^2)]$ is 100 times larger than the second largest eigenvalue (Fig. 5a) 1st row). The contribution of the first eigenvector to the quantity μ_{11} is also dominantly stronger than that from other eigenvectors (Fig. 5a) 2nd row). However, by comparing the diagonal elements of μ_{11} calculated with 4D Fourier transform and the approximations calculated with 2D Fourier transforms (Fig. 5b), we can come to the conclusion that two eigenvectors offer a more accurate approximation. On the other hand, one should bear in mind that due to multiple scattering in the sample, the contrast contributed by pure core-loss scattering can barely be visualized since it is mixed with the contrast contributed by pure elastic scattering. As long as elastic scattering dominates, the 4D matrix for high-loss scattering can still be approximated by one single eigenvector.

As a summary, we have shown that in the example of diagonalizing $S(\vec{q}, \vec{q}', \Delta E)/[(q_E^2 + q^2)(q_E^2 + q'^2)]$ for a crystal, only one eigenvector is sufficient for approximating the original function in the low-loss case. In the core-loss case, if the contrast introduced by inelastic scattered

electrons matters, for example in core-loss EFTEM imaging, then more than one eigenvector is preferred. Otherwise, a single eigenvector suffices in this case as well. As a result, 4D Fourier transforms can be replaced by the same number of 2D Fourier transforms. In the multislice calculation involving inelastic scattering, the computational efficiency can be improved dramatically.

4. Discussions

4.1. The number of necessary eigenvectors required to reconstruct the matrix

The entanglement of two states ϕ_1 and ϕ_2 can be written in the form of correlation - $\phi_1^*\phi_2$. If the entangled state can still be factorized into the original two pure states, then we obtain

$$\phi_1^*\phi_2 = \phi_1\phi_2. \quad (19)$$

Eq. (19) holds true only if ϕ_1 and ϕ_2 are simultaneously delta functions or constants. They can differ from each other by a scaling factor. As a result, the entangled state $\phi_1^*\phi_2$ is either a delta function or a constant, simply the overlap of pure states. The eigenvectors of the matrix $S(\vec{q}, \vec{q}', \Delta E)/[(q_E^2 + q^2)(q_E^2 + q'^2)]$ can be interpreted as a group of orthogonal states. The matrix itself is hence an incoherent summation of overlapping pure states $\phi_n\phi_n^*$. A bold surmise would be that the number of eigenvectors required to represent the matrix depends on the extent of coherence of the matrix. If the matrix resembles a delta function or is close to a constant, then it is highly coherent and only a few or even one eigenvector is required to decompose the matrix.

One can justify this surmise by comparing the profiles of the diagonal elements of the matrix $S(\vec{q} = \vec{q}', \Delta E = 10 \text{ eV})/[(q_E^2 + q^2)(q_E^2 + q'^2)]$ for a single carbon atom (Fig. 1b) blue curve) and for graphene (Fig. 3b) blue curve). Since μ_{11} is proportional to the Fourier transform of the 4D matrix $S(\vec{q}, \vec{q}', \Delta E)/[(q_E^2 + q^2)(q_E^2 + q'^2)]$, a flat profile of μ_{11} implies that the 4D matrix is characterized by a sharp peak. Therefore, we can deduce that $S(\vec{q} = \vec{q}', \Delta E = 10 \text{ eV})/[(q_E^2 + q^2)(q_E^2 + q'^2)]$ is much more convergent for graphene than for a single carbon atom. It has been shown in Section 3 that only one eigenvector is required to approximate the 4D matrix in the case of graphene, while four are necessary in the case of a single carbon atom. Our conjecture is therefore confirmed.

4.2. Eigenvectors of a single atom

Schattschneider et al. have shown that the first-order Born approximation of the MDFF for a single atom can be expanded in the form of spherical harmonics [23]. Löffler has decomposed the MDFF of a single atom with the basis of spherical harmonics under the Kohn-Sham approximation [18]. Based on the calculations following the Raman-Compton model (Figs. 1a, 2a), we have shown that the eigenvectors of the matrix $S(\vec{q}, \vec{q}', \Delta E)/[(q_E^2 + q^2)(q_E^2 + q'^2)]$ resemble spherical harmonics in the case of a single atom. In this discussion we want to demonstrate that the patterns in Figs. 1a, 2a) are indeed related to spherical harmonics.

The first term of the MDFF of a single atom based on the Raman-Compton model (Eq. (10)) is the Fourier transform of the electron density $n_e(r)$:

$$F(\vec{K} - \vec{K}') = \int n_e(r) e^{-i(\vec{K} - \vec{K}') \cdot \vec{r}} d^3\vec{r}. \quad (20)$$

According to Rayleigh equation and spherical harmonic addition theorem, the terms $e^{-i\vec{K} \cdot \vec{r}}$ can be expanded in the form of spherical harmonics as follows:

$$e^{-i\vec{K} \cdot \vec{r}} = 4\pi \sum_{l=0}^{\infty} \sum_{m=-l}^l (-i)^l j_l(Kr) Y_l^m(\theta_{\vec{K}}, \phi_{\vec{K}}) \bar{Y}_l^m(\theta_{\vec{r}}, \phi_{\vec{r}}). \quad (21)$$

Here $\theta_{\vec{K}}$ and $\phi_{\vec{K}}$ are the altitude angle and azimuthal angle of the

vector \vec{K} ; $\theta_{\vec{r}}$ and $\phi_{\vec{r}}$ are the altitude angle and azimuthal angle of the vector \vec{r} . j_l is the l th-order spherical Bessel function.

By inserting the relation Eq. (21) into Eq. (20), we obtain

$$\begin{aligned} F(\vec{K} - \vec{K}') &= \int n_e(r) e^{-i\vec{K}\cdot\vec{r}} e^{i\vec{K}'\cdot\vec{r}} d^3\vec{r} = \int_0^\infty \int_0^{2\pi} \int_0^\pi n_e(r) \\ &\quad e^{-i\vec{K}\cdot\vec{r}} e^{i\vec{K}'\cdot\vec{r}} r^2 \sin\theta_{\vec{r}} d\theta_{\vec{r}} d\phi_{\vec{r}} dr \\ &= 16\pi^2 \sum_l \sum_{m=-l}^{m=l} \int_0^\infty n_e(r) j_l(Kr) j_l(K'r) Y_l^m(\theta_{\vec{K}}, \phi_{\vec{K}}) \\ &\quad \bar{Y}_l^m(\theta_{\vec{K}'}, \phi_{\vec{K}'}) r^2 dr. \end{aligned} \quad (22)$$

Here the orthogonality of the spherical harmonics with respect to \vec{r} has been used:

$$\int_0^{2\pi} \int_0^\pi Y_l^m(\theta_{\vec{r}}, \phi_{\vec{r}}) \bar{Y}_{l'}^{m'}(\theta_{\vec{r}}, \phi_{\vec{r}}) \sin\theta_{\vec{r}} d\theta_{\vec{r}} d\phi_{\vec{r}} = \delta_{mm'} \delta_{ll'}. \quad (23)$$

By setting $\vec{K}' = 0$ in Eq. (22), we obtain the decomposition of $F(\vec{K})$ in the form of spherical harmonics. Since the spherical Bessel function $j_l(0) = 0$ holds true for any order $l \neq 0$, only the term $l=0$ contributes to the sum in Eq. (22). For $l = m = 0$, we have $j_l(0) = 1$ and $Y_l^m(\theta_{\vec{K}}, \phi_{\vec{K}}) = \bar{Y}_l^m(\theta_{\vec{K}}, \phi_{\vec{K}}) = 1/2\sqrt{\pi}$. Therefore $F(\vec{K})$ reduces to

$$F(\vec{K}) = 4\pi \int_0^\infty n_e(r) j_0(Kr) r^2 dr = cR_0(K). \quad (24)$$

Eq. (24) is simplified as the product of a constant c and a radial function of \vec{K} defined by $R(K)$. Similarly, by setting $\vec{K} = 0$ in Eq. (22), we obtain

$$F(-\vec{K}') = 4\pi \int_0^\infty n_e(r) j_0(K'r) r^2 dr = cR_0(K'). \quad (25)$$

Defining $-c^2/Z = \lambda_0$, we get

$$-\frac{1}{Z} F(\vec{K}) F(-\vec{K}') = \lambda_0 R_0(K) R_0(K'). \quad (26)$$

The integral of Eq. (22) with respect to the radial coordinate r results in a summed products of the radial functions $R_l^n(K)$ and $R_l^n(K')$:

$$16\pi^2 \int_0^\infty n_e(r) j_l(Kr) j_l(K'r) r^2 dr = \sum_n \lambda_n R_l^n(K) R_l^n(K'). \quad (27)$$

By inserting Eq. (27) into Eq. (22), we obtain

$$F(\vec{K} - \vec{K}') = \sum_n \sum_l \sum_{m=-l}^{m=l} \lambda_n R_l^n(K) R_l^n(K') Y_l^m(\theta_{\vec{K}}, \phi_{\vec{K}}) \bar{Y}_l^m(\theta_{\vec{K}'}, \phi_{\vec{K}'}). \quad (28)$$

One can define each eigenfunction of the MDFF (Eq. (10)) as a product of a radial function and an angular function:

$$\phi_N(\vec{K}) = R_l^n(K) Y_l^m(\theta_{\vec{K}}, \phi_{\vec{K}}), \quad (29)$$

$$\phi_N^*(\vec{K}') = R_l^n(K') \bar{Y}_l^m(\theta_{\vec{K}'}, \phi_{\vec{K}'}). \quad (30)$$

Here $N = N(n, l, m)$. Using the relation Eqs. (29)–(30), one can write Eq. (10) as

$$S(\vec{K}, \vec{K}', \Delta E) = p(\Delta E) \sum_N \lambda_N \phi_N(\vec{K}) \phi_N^*(\vec{K}'). \quad (31)$$

Considering that the scattering vector \vec{K} depends on the in-plane reciprocal vector \vec{q} and the energy loss ΔE , we rewrite Eq. (31) as

$$S(\vec{q}, \vec{q}', \Delta E) = p(\Delta E) \sum_N \lambda_N \phi_N(\vec{q}, \Delta E) \phi_N^*(\vec{q}', \Delta E). \quad (32)$$

As a summary, the 4D functions $S(\vec{q}, \vec{q}', \Delta E)$ for a single atom can be decomposed into products of spherical harmonic functions. The eigenvectors of $S(\vec{q}, \vec{q}', \Delta E)/[(q_E^2 + q^2)(q_E^2 + q'^2)]$ is equivalent to multiplying the eigenvectors of $S(\vec{q}, \vec{q}', \Delta E)$ with a factor $1/(q_E^2 + q^2)$. The magnitude of energy loss determines the width of the Lorentzian

function $1/(q_E^2 + q^2)$ and hence how convergent the eigenvectors are. As a result, the eigenvectors of $S(\vec{q}, \vec{q}', \Delta E)/[(q_E^2 + q^2)(q_E^2 + q'^2)]$ for an energy loss of 300 eV are more broadly distributed compared with the ones for an energy loss of 10 eV (Figs. 1 and 2).

Since in the Raman-Compton-Wentzel model, the materials only defines the atomic number Z and the characteristic elastic scattering vector q_A in Eq. (13), our conclusions for carbon-based materials can also be extended to other elements.

4.3. The influence of inelastic scattering at different sample depths on the image contrast

The general multislice algorithm accounting for multiple scattering in the sample is summarized in Eq. (15). When inelastic scattering takes place within a certain slice m , the transmission function for low-loss scattering employs the form of Eq. (18). In the case of core-loss scattering, Eq. (18) can be employed as well, as long as the contrast contributed by core-loss scattering is trivial compared with elastic or low-loss scattering. In contrast to the transmission function for pure elastic scattering (Eq. (16)), the transmission function for inelastic scattering has an extra factor $\frac{\alpha_E \sqrt{b_0}}{\pi \beta} \exp[-\mu_2(\vec{r})] \sqrt{\lambda_1} \phi_1(\vec{r}, \Delta E)$. Based on the calculation in Section 3.2, $\phi_1(\vec{r}, \Delta E)$ is close to a constant for low-loss scattering, and so is $\mu_{11}(\vec{r} = \vec{r}', \Delta E)$. Since the absorption factor $\mu_2(\vec{r})$ is an integral of the quantity $\mu_{11}(\vec{r} = \vec{r}', \Delta E)$ (Eq. (4)), we come to the conclusion that $\mu_2(\vec{r})$ for low-loss scattering is also close to a constant. Therefore in this case, the transmission function $t_m^{(in)}(\vec{r}, \Delta E)$ for low-loss scattering with a certain energy loss ΔE can be approximated by the product of the transmission function $t_m(\vec{r})$ for pure elastic scattering and a constant $c(\Delta E)$. We write it as

$$t_m^{(in)}(\vec{r}, \Delta E) = c(\Delta E) t_m(\vec{r}). \quad (33)$$

As a result, low-loss scattering is incorporated in a multislice algorithm and the scattered wave is calculated as

$$\begin{aligned} \psi_m(\vec{r}) &= [\psi_{m-1}(\vec{r}) \cdot t_m^{(in)}(\vec{r}, \Delta E)] \otimes P(\vec{r}) \approx [\psi_{m-1}(\vec{r}) \cdot c(\Delta E) t_m(\vec{r})] \\ &\quad \otimes P(\vec{r}) = c(\Delta E) [\psi_{m-1}(\vec{r}) \cdot t_m(\vec{r})] \otimes P(\vec{r}). \end{aligned} \quad (34)$$

Eq. (34) indicates that for a monoatomic crystal, it does not matter on which slice low-loss scattering takes place. The final image is equivalent to the image calculated with conventional multislice algorithm considering pure elastic scattering, scaled by a constant $c(\Delta E)$ depending on the energy loss ΔE . For complex crystal however, this constant $c(\Delta E)$ might vary for different sample depths, and all possibilities need to be taken into account.

In order to illustrate our conclusions for monoatomic crystals, we have performed simulations by using one single eigenvector obtained from matrix diagonalization to model inelastic scattering. In one simulation, the electrons are assumed to have propagated through a 20-layered AB-stacking graphite and experienced an energy loss of 10 eV, and in the other simulation electrons are assumed to have propagated through the same sample and suffered an energy loss of 300 eV. The sample thickness is about 6.3 nm since the interlayer distance is 3.35 Å. Two extreme cases are considered - inelastic scattering taking place at the top and bottom layer. In order to optimize the image contrast, a slight underfocus with respect to the bottom layer is taken into account and therefore an extra defocus of 7 nm is employed in the simulations.

Based on our simulations in the middle plots of Fig. 6, it makes no difference whether the inelastic scattering takes place at the top layer or at the bottom layer for an energy loss of 10 eV. In order to test the accuracy of our approximation using one eigenvector to model the inelastic scattering, we have performed an extra simulation using the 4D matrix involving MDFF for modelling the inelastic scattering (Fig. 6 middle, green dash curve). The number of 4D Fourier transforms is minimized by assuming that the inelastic scattering takes place at the

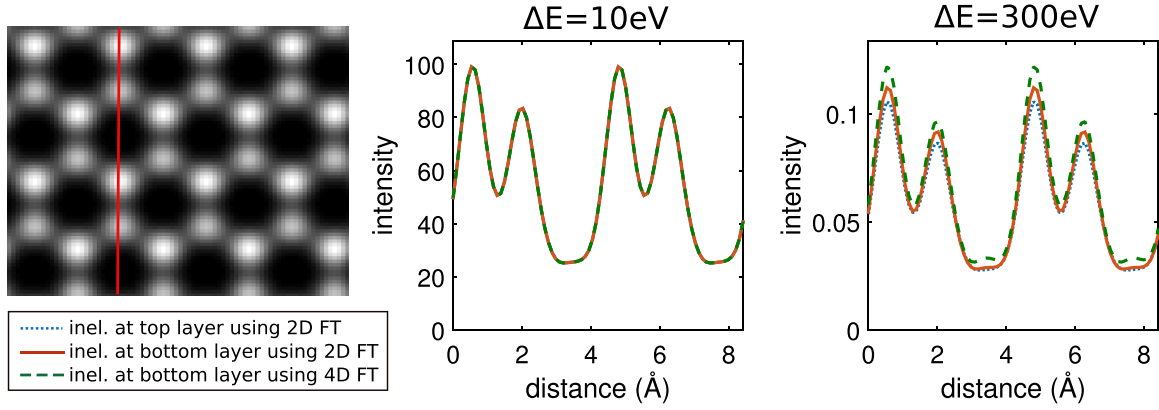


Fig. 6. The influence of inelastic scattering on the image contrast simulated for TEM operated at 20 kV. Inelastic scattering is assumed to take place at top or bottom layer of a 20-layered graphite (6.3 nm thick). The bar in the left image marks the the position where line profiles are measured. The middle and right plots show calculations for 10 eV-loss scattering and for 300 eV-loss scattering, respectively. There are three line profiles shown in each plot - 1. green dash: calculated directly with the 4D matrix $S(\vec{q}, \vec{q}', \Delta E)/[(q_E^2 + q^2)(q_E'^2 + q'^2)]$ assuming an inelastic scattering taking place at the bottom layer; 2. blue dots: calculated with only one 2D eigenvector and assuming an inelastic scattering taking place at the top layer; 3. red solid: calculated with only one 2D eigenvector and assuming an inelastic scattering taking place at the bottom layer. Aberration parameters: $\Delta f = 7$ nm, and this corresponds to a slight underfocus with respect to the bottom layer.

bottom layer. The perfect match between the curves calculated with 4D matrix and one of its 2D eigenvector shows that one eigenvector offers a rather accurate approximation for describing low-loss scattering. After all, since there is only one inelastic scattering event but multiple elastic scattering, elastic contrast dominates in the final image.

According to the image simulation using one single eigenvector for an energy loss of 300 eV, the atom contrast is slightly higher when inelastic scattering takes place at the bottom layer (Fig. 6, right), in contrast to inelastic scattering at the top layer. An explanation is that the contrast resulting from the inelastic scattering at the top surface of the sample is suppressed by the contrast contributed by multiple elastic scattering throughout the sample thickness. An extra calculation using the complex 4D matrix has been employed to test the accuracy of the approximation by one eigenvector in image simulation for the core-loss case. The number of 4D Fourier transforms is minimized by presuming that the core-loss scattering takes place at the bottom layer. From the comparison between the green dashed curve and the red solid curve in the right image in Fig. 6, we come to the conclusion that one eigenvector can approximate the 4D matrix with sufficient degree of accuracy. Especially when all electrons are collected for imaging, elastic contrast dominates and the contrast contributed by core-loss scattering is negligible.

5. Summary and outlook

We have illustrated that by utilizing the method of matrix diagonalization, one can find proper basis to accurately reconstruct the function $S(\vec{q}, \vec{q}', \Delta E)/[(q_E^2 + q^2)(q_E'^2 + q'^2)]$, a four-dimensional quantity used for

modelling inelastic scattering. With this method, not only can a four-dimensional problem be reduced to a two-dimensional problem, but the number of two-dimensional problems is also minimized. In our examples for a single carbon atom scattering a 20 keV electron, one needs four eigenvectors to accurately approximate the function $S(\vec{q}, \vec{q}', \Delta E)/[(q_E^2 + q^2)(q_E'^2 + q'^2)]$, while only one eigenvector provides sufficient accuracy for the approximation in the case of scattering in a crystal. This can be a great advantage when one encounters the problem of multiple inelastic scattering in a thick object. A single inelastic scattering event results in a number of 4D mutual coherence functions, and instead of performing many 4D Fourier transforms, one only needs to perform the same number of 2D Fourier transforms. In the case of multiple inelastic scattering, the number of generated mutual coherence functions increases exponentially, which indicates that the number of 4D Fourier transforms can be overloaded for the computer. In this case, the efficiency improvement through the 2D Fourier transforms helps us to study more complicated scattering problems.

Acknowledgments

We wish to give our sincere thanks to Dr. Stephan Löffler and Prof. Dr. Helmut Kohl for the discussions, based on which we got the inspiration for this work. We also want to acknowledge the financial support of DFG (German Research Foundation) and the Ministry of Science, Research and the Arts (MWK) of Baden-Württemberg in the frame of the (Sub-Angstrom Low-Voltage Electron microscopy) (SALVE) project (Grant number: KA1295/21-1).

Appendix A. Diagonalization of a four-dimensional Hermitian matrix

A two-dimensional symmetric or Hermitian matrix M can be diagonalized as

$$M = \sum_n \lambda_n x_n x_n^{*T} = \begin{pmatrix} x_1 & x_2 & \cdots & x_n \end{pmatrix} \begin{pmatrix} \lambda_1 & 0 & \cdots & 0 \\ 0 & \lambda_2 & \cdots & 0 \\ \vdots & \vdots & \ddots & \vdots \\ 0 & 0 & \cdots & \lambda_n \end{pmatrix} \begin{pmatrix} x_1^{*T} \\ x_2^{*T} \\ \vdots \\ x_n^{*T} \end{pmatrix}. \quad (\text{A.1})$$

Here the *eigenvector* x_n is a column vector and therefore x_n^{*T} is a row vector. For a symmetric matrix, $x_n = x_n^*$ and the eigenvalue λ_n is real. All eigenvectors are orthonormal to each other and therefore satisfy

$$x_m^{*T} x_n = \begin{cases} 0 & \text{if } m \neq n \\ 1 & \text{if } m = n \end{cases} \quad (\text{A.2})$$

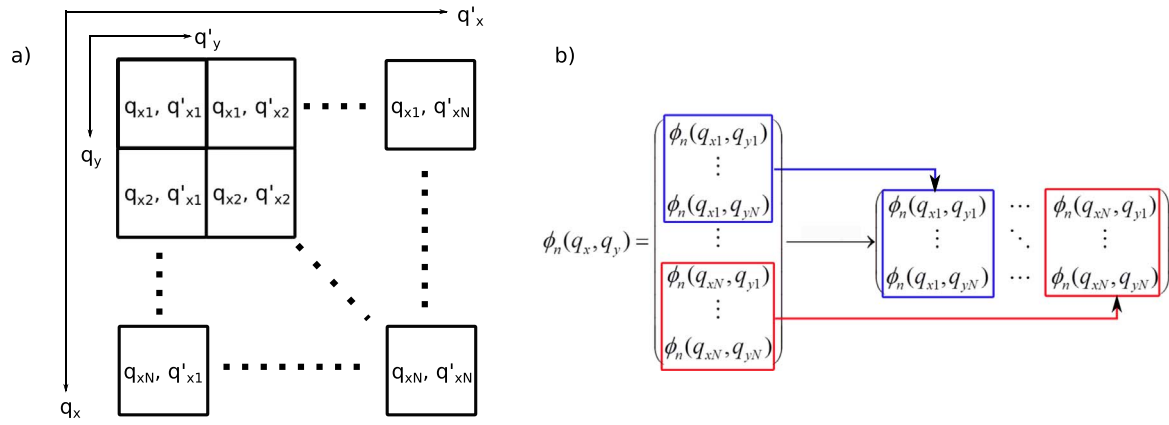


Fig. A. 1 The illustration shows: a) How a 4D array of the size $N \times N \times N \times N$ is ‘flattened’ into a $N^2 \times N^2$ 2D matrix. Each small square represents a $N \times N$ matrix (q_y, q'_y) for a pair of fixed q_x and q'_x . b) How one eigenvector $\phi_n(q_x, q_y)$ retrieved from the diagonalization of the flattened matrix in a) is restored back to two dimensions.

In order to decompose a 4D Hermitian array $M(\vec{q}, \vec{q}')$, where \vec{q} and \vec{q}' are both 2D vectors and which satisfies $M(\vec{q}, \vec{q}') = M^*(\vec{q}', \vec{q})$, we flatten the 4D array into a 2D matrix by adapting the following method: (i) Firstly, the 4D array is written in the Cartesian coordinates $\vec{q}_x, \vec{q}_y, \vec{q}'_x$ and \vec{q}'_y :

$$M(\vec{q}, \vec{q}') = M(q_x, q_y, q'_x, q'_y). \quad (\text{A.3})$$

(ii) Secondly, the 2D representation of $M(q_x, q_y, q'_x, q'_y)$ is denoted by

$$S_{N(j-1)+k, N(m-1)+n} = S(q_{xj}, q_{yk}, q'_{xm}, q'_{yn})j, k, m, n = 1, 2, 3 \dots N. \quad (\text{A.4})$$

Here $N(j-1) + k$ and $N(m-1) + n$ are the row number and column number of an element in the flattened matrix, respectively. The 4D array $M(q_x, q_y, q'_x, q'_y)$ is of the size $N \times N \times N \times N$, and the flattened matrix M is therefore of the size $N^2 \times N^2$, shown in Fig. A.1.a). The diagonalization of the 2D matrix M can therefore be written as:

$$M(\vec{q}, \vec{q}') = \sum_n \lambda_n \phi_n(\vec{q}) \phi_n^{*T}(\vec{q}') = (\phi_1(\vec{q}) \quad \phi_2(\vec{q}) \quad \dots \phi_n(\vec{q})) \begin{pmatrix} \lambda_1 & 0 & \dots & 0 \\ 0 & \lambda_2 & \dots & 0 \\ \vdots & \vdots & \ddots & \vdots \\ 0 & 0 & \dots & \lambda_n \end{pmatrix} \begin{pmatrix} \phi_1^{*T}(\vec{q}') \\ \phi_2^{*T}(\vec{q}') \\ \vdots \\ \phi_n^{*T}(\vec{q}') \end{pmatrix}. \quad (\text{A.5})$$

Here the eigenvectors satisfy $\phi_n(\vec{q}) = \phi_n(\vec{q}')$ and orthonormal to each other:

$$\phi_m^{*T}(\vec{q}') \phi_n(\vec{q}) = \delta_{mn}. \quad (\text{A.6})$$

(iii) As the last step, we reshape the eigenvectors from 1D back to 2D, as shown in Fig. A.1b).

References

- [1] R.J. Glauber, High energy collision theory, *Lect. Theor. Phys.* 1 (S 315) (1959).
- [2] A. Howie, Inelastic scattering of electrons by crystals i. the theory of small-angle inelastic scattering, in: *Proceedings of the Royal Society of London A: Mathematical, Physical and Engineering Sciences*, vol. 271, 1963, pp. 268–287.
- [3] John M. Cowley, A. F. Moodie, The scattering of electrons by atoms and crystals. i. a new theoretical approach, *Acta Crystallogr.* 10 (10) (1957) 609–619.
- [4] H. Rose, Image formation by inelastically scattered electrons in electron microscopy, *Optik* 45 (1976) 139–158.
- [5] H. Rose, Information transfer in transmission electron microscopy, *Ultramicroscopy* 15 (1984) 173–191.
- [6] H. Kohl, H. Rose, Theory of image formation by inelastically scattered electrons in the electron microscope, *Adv. Electron. Electron. Phys.* 65 (1985) 173–227.
- [7] S.L. Dudarev, L.M. Peng, M.J. Whelan, Correlations in space and time and dynamical diffraction of high-energy electrons by crystals, *Phys. Rev. B* 48 (18) (1993) 13408–13429. <http://dx.doi.org/10.1103/physrevb.48.13408>.
- [8] P. Schattschneider, Density matrix of inelastically scattered fast electrons, *Phys. Rev. B* 59 (1999) 10959–10969.
- [9] C. Dinges, A. Berger, H. Rose, Simulation of TEM images considering phonon and electronic excitations, *Ultramicroscopy* 60 (1) (1995) 49–70.
- [10] H. Müller, H. Rose, P. Schorsch, A coherence function approach to image simulation, *J. Microsc.* 190 (1–2) (1998) 73–88 (ISSN 1365-2818).
- [11] C. Dwyer, Multislice theory of fast electron scattering incorporating atomic inner-shell ionization, *Ultramicroscopy* 104 (2005) 141–151.
- [12] M.A.L. Marques, Eberhard K.U. Gross, Time-dependent density functional theory, *Annu. Rev. Phys. Chem.* 55 (2004) 427–455. <http://dx.doi.org/10.1146/annurev-physchem.55.091602.094449>.
- [13] Zachary H. Levine, Diffraction and electron energy loss to plasmons in silicon slabs, *Phys. Rev. B* 77 (2008) 125314. <http://dx.doi.org/10.1103/physrevb.77.125314>.
- [14] C. Dwyer, The role of symmetry in the theory of inelastic high-energy electron scattering and its application to atomic-resolution core-loss imaging, *Ultramicroscopy* 151 (2015) 68–77.
- [15] Leslie J. Allen, Adrian J. D’Alfonso, S.D. Findlay, Modelling the inelastic scattering of fast electrons, *Ultramicroscopy* 151 (2015) 11–22.
- [16] J. Verbeeck, P. Schattschneider, A. Rosenauer, Image simulation of high resolution energy filtered TEM images, *Ultramicroscopy* 109 (2009) 350–360.
- [17] N.R. Lugg, B. Freitag, S.D. Findlay, L.J. Allen, Energy-filtered transmission electron microscopy based on inner-shell ionization, *Ultramicroscopy* 110 (2010) 981–990.
- [18] Stefan Löffler, Viktoria Motsch, Peter Schattschneider, A pure state decomposition approach of the mixed dynamic form factor for mapping atomic orbitals, *Ultramicroscopy* 131 (2013) 39–45.
- [19] Z. Lee, H. Rose, R. Hambach, P. Wachsmuth, U. Kaiser, The influence of inelastic scattering on EFTEM images-exemplified at 20 kV for graphene and silicon, *Ultramicroscopy* 134 (0) (2013) 102–112.
- [20] Ray F. Egerton, *Electron Energy-Loss Spectroscopy in The Electron Microscope*, Springer, 2011.
- [21] Gr. Wentzel, Zwei Bemerkungen über die zerstreung korpuskularer strahlen als beugungserscheinung, *Z. für Phys. A Hadrons Nucl.* 40 (8) (1926) 590–593.
- [22] Daniela Calvetti, L. Reichel, Danny Chris Sorensen, An implicitly restarted lanczos method for large symmetric eigenvalue problems, *Electron. Trans. Numer. Anal.* 2 (1) (1994) 21.
- [23] Peter Schattschneider, Stefano Rubino, Cécile Hébert, J. Ruzs, J. Kuneš, P. Novák, E. Carlino, M. Fabrizio, G. Panaccione, G. Rossi, Detection of magnetic circular dichroism using a transmission electron microscope, *Nature* 441 (7092) (2006) 486–488.